Journal of Power Sources 630 (2025) 236073

Contents lists available at ScienceDirect

Journal of Power Sources

journal homepage: www.elsevier.com/locate/jpowsour

Ternary electrolyte additive mixture for 5V lithium-ion battery cells

Markus Binder[a,b], Matthias Kuenzel[a,b], Thomas Diemant[a,b], Zenonas Jusys[a,b,c], R.Jürgen Behm[c], Joachim R. Binder[d], Sandro Stock[e], Felix Diller[e], Rüdiger Daub[e], Stefano Passerini[b,**], Dominic Bresser[a,b,*]

[a] Helmholtz Institute Ulm (HIU), Helmholtzstr. 11, D-89081, Ulm, Germany
[b] Karlsruhe Institute of Technology (KIT), D-76021, Karlsruhe, Germany
[c] Institute of Theoretical Chemistry, Ulm University, Oberberghof 7, D-89081, Ulm, Germany
[d] Institute for Applied Materials (IAM), KIT, D-76344, Eggenstein-Leopoldshafen, Germany
[e] Institute for Machine Tools and Industrial Management, Technical University of Munich (TUM), D-85748, Garching, Germany

HIGHLIGHTS

- Stabilized interphases at the positive and negative electrode.
- Mitigated transition metal cross-talk.
- Reduced gas evolution upon cycling and storage.
- Fully aqueous processed graphite||$LiNi_{0.5}Mn_{1.5}O_4$ lithium-ion cells.

GRAPHICAL ABSTRACT

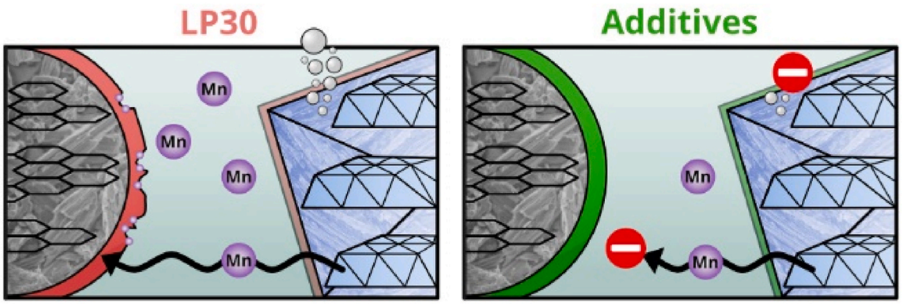

ARTICLE INFO

Keywords:
Electrolyte
Additives
Aqueous processing
High-voltage cathode
Lithium-ion battery

ABSTRACT

Cobalt-free $LiNi_{0.5}Mn_{1.5}O_4$ (LNMO) is a promising alternative to the commonly used cobalt-containing positive electrode active materials in lithium-ion batteries (LIBs), owing to its high redox potential, relatively low cost, and low environmental impact. The high cell voltage, however, comes along with several challenges that need to be overcome before the material can be successfully used in commercial cells. Herein, these challenges are addressed by introducing three additives into the liquid organic carbonate-based electrolyte, namely tris (trimethylsilyl)-phosphite (TTSPi), lithium bis(oxalato) borate (LiBOB), and ethyl-(2,2,2-trifluoroethyl) carbonate (TFEC). The optimized electrolyte composition enables superior performance of Li||LNMO and graphite||LNMO cells because of the stabilized interphases at both the negative and the positive electrode and, thus, suppressed electrolyte decomposition. This is demonstrated by the substantially reduced gassing upon cycling and shelf-storage. These results are anticipated to contribute to the successful commercialization of LNMO in more sustainable LIBs.

---

* Corresponding author. Helmholtz Institute Ulm (HIU), Helmholtzstr. 11, D-89081, Ulm, Germany.
** Corresponding author.
E-mail addresses: stefano.passerini@kit.edu (S. Passerini), dominic.bresser@kit.edu (D. Bresser).

https://doi.org/10.1016/j.jpowsour.2024.236073
Received 7 August 2024; Received in revised form 23 November 2024; Accepted 11 December 2024
Available online 19 December 2024

1. Introduction

Lithium-ion batteries (LIBs) are the dominating electrochemical energy storage technology for powering portable electronic devices and (hybrid) electric vehicles [1–4]. With the wide-spread use of LIBs, however, the cost and environmental impact of LIBs have increasingly come into focus. Concerning the positive electrode, as a major cost factor for LIBs, two approaches to address these issues imply the use of aqueous electrode processing for the positive electrode – as already well established for graphite-based negative electrodes – and the reduction/elimination of costly elements such as cobalt [5–7]. Concerning the latter, spinel-structured $LiNi_{0.5}Mn_{1.5}O_4$ (LNMO) is among the most promising alternatives beside already commercially used $LiFePO_4$ [8]. While the high de-/lithiation potential of about 4.7 V is beneficial for the achievable energy density, it imposes a great challenge on the electrolyte, since this is well beyond the electrochemical stability window of state-of-the-art carbonate-based liquid electrolytes, which decompose at potentials above 4.3 V vs. Li^+/Li [9,10]. Different from graphite anodes, where a stable solid electrolyte interphase (SEI) forms at the electrode|electrolyte interface [11], the electrolyte decomposition on LNMO results in the formation of an unstable cathode electrolyte interphase (CEI) that does not inhibit further electrolyte decomposition during cycling [12–15]. In addition, especially in the presence of small quantities of water (e.g., as a result of the aqueous processing or simply an insufficiently dried electrolyte), the electrolyte decomposition leads to the formation of highly corrosive and toxic HF and $H_xPO_yF_z$ [16–19]. Amongst others, these acidic species promote the dissolution of the transition metals from the positive electrode, which is not only an issue for the cathode active material itself, but also results in manganese migration to the anode, where it leads to the breakdown of the stable SEI on graphite [18,20,21].

In order to stabilize the SEI and CEI, and to reduce the amount of detrimental acidic species in the cell, the use of electrolyte additives is a cost-efficient and easy to implement approach for commercial cell manufacturing [22–27]. One of many individually studied additives for high-voltage battery cells is tris(trimethylsilyl)-phosphite (TTSPi) [16,17,28–31]. Several studies showed the beneficial effect of TTSPi on the electrochemical performance due to the formation of a protective CEI [17,30], a decreased cell impedance [29], and the ability of scavenging HF [17,32]. These advantageous effects were also observed when TTSPi was combined with other additives such as vinylene carbonate (VC) [29] or methylene methanedisulfonate (MMDS) [31]. Another well-studied electrolyte additive is lithium bis(oxalato)borate (LiBOB) [33–38]. LiBOB does not only serve as an additional lithium source, but further leads to the incorporation of oligoborates into the CEI [35–37] and SEI [22,33,34]. In contrast to TTSPi, which shows scavenging properties towards acidic species like HF, adding LiBOB to the electrolyte addresses this issue more at its root by preventing the actual formation of HF via binding to the PF_5 intermediate [34]. An additional class of electrolyte additives that has received a lot of attention in the past years are partially fluorinated carbonates, e.g., bis(2,2,2-trifluoroethyl) carbonate (TFEC) [25,39–45]. In addition to an enhanced overall performance, these additives have been reported to enable a stabilized interface between the aluminum current collector and the electrolyte, and to favor the formation of an enhanced SEI [46] and CEI [47] as a result of a modified lithium salt coordination, thus, favoring the formation of rather inorganic than organic interphases.

In a recent study, we investigated the combination of all three additives, i.e., TTSPi, TFEC, and LiBOB for graphite||LNMO cells and observed an improved cycling performance in terms of achievable specific capacity and cycling stability – without investigating the origin of this advantageous effect, though [32]. When considering such advanced electrolyte compositions for commercial use, however, another important impact factor is the gassing behavior. In fact, Song et al. [48] reported an enhanced cycling stability for graphite||$LiNi_{0.8}Mn_{0.1}Co_{0.1}O_2$ cells when combining lithium difluoro(dioxalato)phosphate (LiDFDOP), fluoroethylene carbonate (FEC), and vinylene carbonate (VC) as electrolyte additives, but this superior performance came along with an increased gassing during cycling.

Following these studies, herein, we investigate the beneficial impact of combining TTSPi, TFEC, and LiBOB in more detail, specifically the impact on the CEI and SEI formation and composition as well as the impact on the gassing behavior when used with high-voltage (Fe- and Ti-doped) LNMO. The findings reveal a highly beneficial effect of this ternary additive mixture on the performance and, at least as important, on the gas evolution, which is substantially reduced and takes place only during the initial cycles, thus, contributing to the potential commercial use of Co-free, high-voltage LNMO in more sustainable next-generation LIBs.

2. Experimental section

2.1. LNMO synthesis

Fe- and Ti-doped LNMO ($LiNi_{0.5}Mn_{1.37}Fe_{0.1}Ti_{0.03}O_4$; hereinafter for simplicity reasons solely referred to as LNMO) was synthesized using a two-step spray drying method with a ball milling step in-between [49,50]. The starting materials were $Li(OOCCH_3) \bullet 2H_2O$ (Acros Organics), $Mn(OOCCH_3)_2 \bullet 4H_2O$ (Sigma-Aldrich), $Ni(OOCCH_3)_2 \bullet 4H_2O$, $Fe(NO_3)_3 \bullet 9H_2O$ (Alfa Aesar), and $Ti(OCH(CH_3)_2)_4$ (Merck). After spray drying the initial solution, the resulting precursor was calcined at 500 °C and 800 °C (2 h for each step). To obtain spherical secondary particles, the powder was ground, spray-dried, and finally sintered at 850 °C for 2 h. The resulting powder consisted of spherical secondary particles composed of well-defined octahedral primary particles [49,50].

2.2. Electrode preparation

The electrode composition was 87 wt% LNMO, 10 wt% conductive carbon (Imerys CNERGY Super C45), and 3 wt% binder. For the electrode preparation, guar gum (Lamberti) and citric acid (CA; 99 %, Sigma-Aldrich) were dissolved in deionized water in a 9:1 ratio, with the CA serving as crosslinker to enhance the mechanical properties of the electrodes and enable an improved cycling performance [51,52]. After adding the Fe- and Ti-doped LNMO and the conductive carbon, phosphoric acid (PA; ortho-phosphoric acid 85 %, with >99 % purity, Bernd Kraft; 1 wt% with respect to the active material) was added and the mixture was homogenized by planetary ball milling for 1.5 h. The addition of PA lowers the pH value of the aqueous electrode slurry and enables the formation of a protective metal phosphate surface layer on the active material particles and the aluminum current collector [52,53]. The resulting slurry was cast on carbon-coated aluminum foil (thickness: 20 μm; battery grade) with a laboratory doctor blade (wet film thickness: 120 μm) and pre-dried in an atmospheric oven (ED-115, Binder) for 15 min at 80 °C. After further drying overnight in a dry room (with a dew point of about −70 °C), disc-shaped electrodes were punched from the electrode tape (geometric area 1.13 cm^2) and pressed at 5 t for 15 s before being dried once again under vacuum ($<10^{-3}$ mbar) at 120 °C for 14 h. The active material mass loading of the LNMO electrodes in Li||LNMO cells was 3.2–3.6 mg cm^{-2} and 5.8–6.5 mg cm^{-2} in graphite||LNMO cells. The graphite electrodes comprised 95 wt% graphite (Actilion, Imerys), 2 wt% conductive carbon (CNERGY Super C45, Imerys), 1 wt% carboxymethyl cellulose (CMC; Walocel CRT 2000, degree of substitution: 0.7, Dow Wolff Cellulosics), and 2 wt% styrene-butadiene rubber (SBR; TRD102A, JSR). The slurry was prepared by magnetic stirring in deionized water and cast onto copper foil (thickness: 10 μm, battery grade) using a laboratory-scale doctor blade.

2.3. Electrochemical characterization

Three-electrode Swagelok® cells, employing lithium-metal foil (thickness: 500 μm, battery grade, Honjo) or graphite-based electrodes as counter electrode and lithium-metal foil as reference electrode, were used for the electrochemical characterization. The cell assembly was carried out in an argon-filled glove box (MBraun, H_2O and O_2 content lower than 0.1 ppm), using glass fiber sheets (Whatman GF/D) as separator. The latter was soaked with 130 μL of the electrolyte. As reference electrolyte, we used LP30 (UBE), i.e., a 1M solution of $LiPF_6$ in ethylene carbonate (EC) and dimethyl carbonate (DMC) (1:1 by weight). Following the previous optimization of the electrolyte composition [32,35], for the additive-containing electrolyte (LP30+Add), 2 wt% TTSPi (>95 %, TCI Chemicals), 1 wt% LiBOB (Sigma-Aldrich), and 0.5 wt% TFEC (98 %, ABCR) were added to LP30. Galvanostatic cycling was performed within the potential range from 3.5 to 4.95 V for the Li||LNMO cells and from 2.8 to 5.0 V for the graphite||LNMO cells. All electrochemical measurements were conducted at 20 ± 2 °C, utilizing a Maccor Battery Tester 4300. A dis-/charge rate of 1C corresponds to a specific current of 147 mA g^{-1}. For the quantitative investigation of the gas evolution, pouch cells were assembled in the dry room. In this case, the electrodes had a surface area of 9 cm^2 (LNMO electrodes) and 10.9 cm^2 (graphite electrodes). The pouch cells contained 1 mL of electrolyte.

2.4. Analysis of the interfaces and interphases

Ex situ X-ray photoelectron spectroscopy (XPS) analysis of the pristine and cycled LNMO and graphite electrodes was performed using a Specs XPS system with a Phoibos 150 energy analyzer. The spectra were acquired using monochromatized Al Kα radiation (400 W, 15 kV) with pass energies of 90 eV and 30 eV for the survey and the detail measurements, respectively. When necessary, sample charging was neutralized with an electron flood gun. The spectra were calibrated to the main C 1s peak at 284.6 eV of the conductive carbon component. To avoid surface contamination, the samples were transferred under inert gas atmosphere from the glove box to the sample load lock of the XPS system. Peak fitting of the XPS spectra was performed with the CasaXPS software package, using Shirley-type backgrounds and Gaussian-Lorentzian peak shapes.

2.5. Analysis of the gassing behavior

Gas evolution measurements were performed in a custom-built immersion bath using Archimedes' principle [54,55]. More precisely, the graphite||LNMO cells were fully immersed in silicone oil (density 0.88 g cm^{-3} , Korasilon TT2, Kurt Obermeier) and attached to a high-precision balance (accuracy 0.1 mg, Sartorius CPA224S). The pouch cells were connected to a BaSyTec CTS battery tester using tiny copper wires ($\phi = 100\ \mu m$) to minimize the influence of the electrical contacts on the measurement. The complete setup was contained inside a climate chamber (Binder ED-115) at a controlled temperature of 20 ± 2 °C as shown in Fig. S1. The measurement principle is based on the buoyancy force, which depends on the mass of the displaced fluid m_{fluid}:

$$F_{buoyant} = m_{fluid}g = \rho Vg$$

where g is the gravitational acceleration, ρ is the mass density of the fluid, and V the displaced volume.

Subsequently, an equilibrium of the forces acting on the cell can be calculated, resulting in a balance between the change of the tension force and the buoyancy force:

$$\Delta F_{tension} = -\Delta F_{buoyant} = -\rho g \Delta V$$

This equation can be simplified to a relation between the volume change of the pouch cell and the recorded mass $\Delta m_{balance}$ of the balance:

$$\Delta V = -\frac{\Delta m_{balance}}{\rho}$$

Hence, a direct, time-resolved measurement was obtained by tracking the readout of the balance. To analyze the gas evolution upon dis-/charge, galvanostatic cycling was performed within a potential range from 2.8 to 5.0 V at a dis-/charge rate of C/5. Data points were recorded every 10 s and the OCV was tracked for at least 3 h following the galvanostatic cycling. For further details about the experimental setup and the validation of the method, the interested reader is referred to previous studies [56,57].

For the differential electrochemical mass spectrometry (DEMS) measurements, the LNMO active material was coated via the doctor-blade method onto a fluorinated ethylene propylene (FEP) membrane, which was sputter-coated with a thin layer of aluminum (~40 nm) to provide a reliable electronic contact. Since this membrane is hydrophobic, an NMP-based slurry with poly-vinylidene difluoride (PVdF, Solef 6020, Solvay) as binder was used. The resulting gas-permeable electrodes were dried at 120 °C and pressed with 5 tons per cm^2. The electrodes had a diameter of 13 mm and were assembled in Swagelok-type T-shaped half-cell. An illustration of the experimental setup is depicted in Fig. S2 and a detailed description can be found in a previous publication [58]. All measurements were performed against lithium-metal counter and reference electrodes using cyclic voltammetry (CV), simultaneously tracking selected mass signals. The CVs were measured with a sweep rate of 2 mV s^{-1}, and IR drop compensation was employed to counter Ohmic losses (170 Ω for LP30 and 70 Ω for LP30+Add).

3. Results and discussion

3.1. Galvanostatic cycling of Li||LNMO and Graphite||LNMO cells

Firstly, we subjected Li||LNMO cells containing the reference electrolyte LP30, i.e., the additive-free electrolyte, and Li||LNMO cells containing the electrolyte with the ternary additive mixture to galvanostatic cycling (Fig. 1). The comparison of the cells employing the reference LP30 electrolyte and that including the ternary additive mixture (LP30+Add) over 1000 dis-/charge cycles at a rate of 1C reveals a significant performance improvement for the latter electrolyte (Fig. 1a). While the reference cells lost 19.5 % of their initial capacity and therefore were close to the standard end-of-life (EOL) threshold of 80 % capacity retention after 1000 cycles [59], the cells employing the additives showed a superior capacity retention of nearly 95 %. The greater capacity retention originates from a more stable and higher average Coulombic efficiency (CE) of 99.8 % for LP30+Add compared to 99.4 % for LP30. The latter, in fact, shows some fluctuation of the CE after about 500 cycles, while this is substantially delayed and reduced for LP30+Add, indicating a suppressed occurrence of side reactions at the lithium-metal counter electrode in the presence of the three additives. It is important to note that the ternary additive mixture generally outperforms the binary mixture of TTSPi and TFEC, which had been the focus in our previous study [32]. According to the literature,[35–37,60] the introduction of LiBOB reinforces the CEI and reduces detrimental side reactions, leading to higher capacity, CE, and capacity retention. As a result, the use of this ternary additive composition leads to a rather stable cycling for more than 3000 cycles at 1C with about 80 % capacity retention (Fig. 1b). The capacity shows some fluctuation after around 2000 cycles, though, which we may assign to the substantial changes of the lithium-metal counter electrode upon such extended cycling. The corresponding dQ/dV profiles are depicted in Fig. 1c and d for LP30 (every 200th cycle) and LP30+Add (every 500th cycle), respectively. In both cases, distinct peaks for the Ni^{2+}/Ni^{3+} and the Ni^{3+}/Ni^{4+} redox processes are visible. When additive-free LP30 is used as the electrolyte (Fig. 1c), however, the oxidation and reduction peaks shift away from each other upon cycling, i.e., the peak separation ΔE_p is increasing, which points at an increasing cell resistance (from $\Delta E_p = 0.035$ V at the beginning to $\Delta E_p = 0.05$ V after 1000 cycles). This is not the case for LP30+Add (Fig. 1d), for which rather the opposite behavior is observed between the 500th cycle (darkest) and the 1,000th cycle (from $\Delta E_p = 0.028$ V to $\Delta E_p = 0.02$ V), indicating that the additive-reinforced CEI

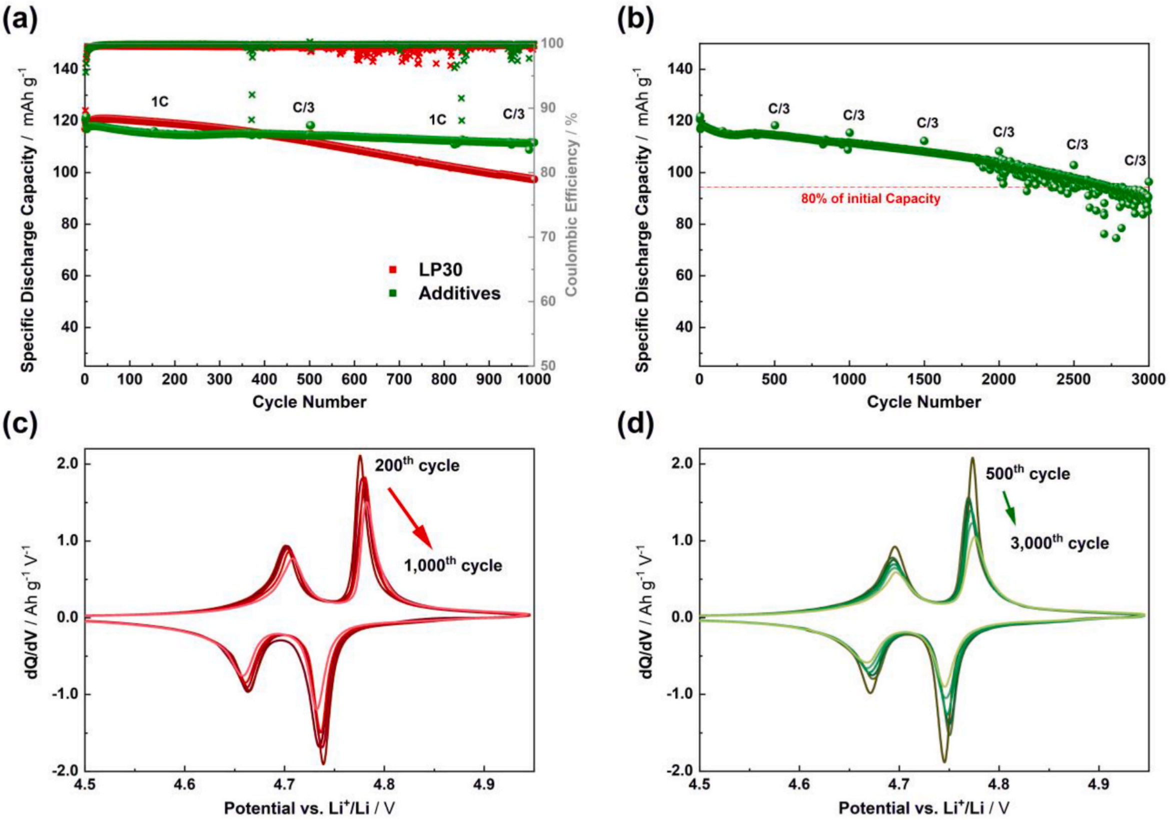

Fig. 1. (a) Specific discharge capacity and Coulombic efficiency of Li||LNMO cells containing LP30 (red) and LP30+Add (green) as the electrolyte upon galvanostatic cycling at a dis-/charge rate of 1C with fingerprint cycles at C/3 every 500 cycles. The cells were cycled at 20 °C between 3.5 and 4.95 V. (b) Specific discharge capacity of Li||LNMO cell containing LP30+Add upon prolonged cycling under the same conditions. (c) Differential capacity during dis-/charge cycling of the LP30 cell for 1000 cycles at 1C depicting every 200th cycle in the potential region of the Ni^{2+}/Ni^{4+} redox couple. (d) Differential capacity during dis-/charge cycling of the LP30+Add cell for 3000 cycles at 1C depicting every 500th cycle in the potential region of the Ni^{2+}/Ni^{4+} redox couple. (For interpretation of the references to color in this figure legend, the reader is referred to the Web version of this article.)

leads to a lower resistance for the charge transfer [61]. Upon further cycling, i.e., until the 3,000th cycle, the oxidation and reduction peaks also slightly shift apart, but the observed shift is much less pronounced than for the reference cell, especially considering the substantially longer cycling test ($\Delta E_p = 0.03$ V after 3000 cycles). The dQ/dV plots in Fig. 1c and d thereby underline the beneficial effect of the additive-derived CEI in stabilizing the LNMO surface and limiting the resistance build-up due to electrolyte decomposition and, probably, active material degradation [62,63]. Besides, we may assume that the addition of TFEC is also beneficial for the stabilization of the lithium|electrolyte interface [64,65], which contributes to the superior cycling stability. To avoid the impact of the lithium-metal electrode, we assembled graphite||LNMO cells and subjected these to constant current cycling tests. The results confirm the superior performance in the presence of the ternary additive composition (see Fig. 2 for cycling at 1C and Fig. S4 for cycling at C/3). Similar to the previous results in Li-metal cells, the additive-containing cells showed a stabilized cycling performance and higher average Coulombic efficiency of 99.8 % for LP30+Add compared to 99.6 % for pure LP30 over 500 cycles at 1C. A closer look at the cycling data reveals a rapid capacity loss during the initial cycles in pure LP30, which is certainly due to irreversible lithium losses resulting from the formation of the SEI and CEI layers in the Li-ion cell as highlighted by the relatively lower CE. In fact, such cells have no excess lithium, resulting in the direct impact of the irreversible reactions into capacity fading. In contrast, the irreversible capacity loss is substantially reduced in the LP30+Add electrolyte, where it can be partly compensated also by the addition of LiBOB. Indeed, the LP30+Add cell showed a first cycle CE lower than that of the LP30 reference (inset in

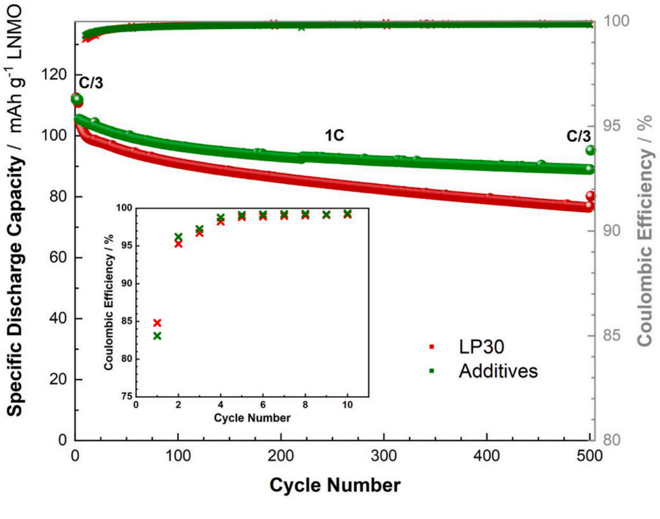

Fig. 2. Specific discharge capacity and Coulombic efficiency of graphite||LNMO cells containing LP30 (red) and LP30+Add (green) as the electrolyte upon galvanostatic cycling at a dis-/charge rate of 1C. The inset shows a magnification of the Coulombic efficiency during the first 10 cycles. The cells were cycled at 20 °C between 2.8 V and 5.0 V. (For interpretation of the references to color in this figure legend, the reader is referred to the Web version of this article.)

Fig. 2), caused by the electrochemical decomposition of the additives to form stable electrode|electrolyte interphases, in turn leading to an improved CE from the second cycle onwards. An *ex situ* SEM analysis of the LNMO cathodes, however, did not reveal any significant difference in presence or absence of the additives (Fig. S3), indicating that also with the additives, the CEI remains in the range of several nanometers and, thus, not detectable by SEM [66].

3.2. *Ex situ XPS analysis of cycled electrodes*

To evaluate the composition of the electrode|electrolyte interphases of cycled electrodes, XPS represents a more suitable technique. For these measurements, we used the electrodes recovered from the graphite||LNMO cells that had been cycled at a C/3 rate for 300 cycles (Fig. S4). The comparison of photographs from the cycled graphite electrodes (left images in Fig. 3) reveals colored deposits on the electrode cycled in LP30, while the graphite electrode from the cell employing LP30+Add still looked comparably fresh. The XPS detail spectra of the Mn 2p region confirms the detrimental migration of significant amounts of manganese to the negative electrode in the reference cell (Fig. 3a) [10,18]. In contrast, the use of the LP30+Add electrolyte led to a substantially reduced amount of Mn deposits to almost zero considering the high sensitivity of XPS measurements. Beside the substantial reduction of manganese migration, the spectra of the F 1s region in Fig. 3b reveal a reduced amount of decomposition products of the lithium salt anion (PF_6^-), namely LiF and $PO_xF_y^{z-}$, on the graphite electrodes in presence of the additives. The significantly lower LiF peak can be attributed to the hindered HF formation by LiBOB [34] and the HF scavenging effect of TTSPi [17]. In combination, this substantially reduces the HF concentration in the electrolyte, thereby suppressing transition metal dissolution at the positive electrode and, in particular, manganese deposition at the negative electrode.

These findings are further supported by the *ex situ* XPS analysis of cycled LNMO cathodes, where the amount of LiF clearly decreased as well for LP30+Add (Fig. 4a). The XPS results in the P 2p region (Fig. 4b) show a much higher contribution of P-O bonds/species for the LNMO electrodes cycled with LP30+Add, which is presumably resulting from the decomposition of TTSPi on the electrode surface (along with the formation of P-F bonds, as apparent from Fig. 4a), leading to the formation of a more stable CEI layer. All of these findings from the XPS analysis are in agreement with previous studies on TTSPi [17] and TTSPi + TFEC [32] containing electrolytes. The influence of the third additive, LiBOB, on the CEI formation on LNMO is evident from the O 1s region (Fig. 4c), showing a significant increase of the amount of C=O groups on the LNMO electrode surface when cycled in LP30+Add compared to pure LP30. This trend, which is in agreement with previous reports [37,60,61], originates from the decomposition of LiBOB, leading to the presence of borate and oxalate species in the CEI. As a matter of fact, the M − O signal from the LNMO lattice is much smaller for the electrode cycled in LP30+Add, indicating the formation of a thicker and/or more homogeneous (and, thus, more stable) CEI covering the LNMO active material particles. This correlates with the lower Coulombic efficiency observed for the 1st cycle of the LP30+Add containing cells (see Fig. 2).

To confirm this correlation, we conducted an additional *ex situ* XPS analysis of LNMO electrodes cycled in a half-cell configuration to three different states of charge during the first delithiation, namely, after resting for 3 h under open circuit condition, after charging to 4.65 V, i.e., the highest voltage where the profiles of both kinds of cells still overlap, and at 4.95 V, i.e., after completing the first delithiation (see also Fig. 5a). From the XPS spectra of the six recovered electrodes (Fig. S5), i.e., a set of three in each electrolyte, trends in the respective surface species can be identified (Fig. 5b), revealing additional valuable insights. First, the comparison of the LNMO lattice M − O signal intensities shows a decrease already in the early stages of the charging process during the first cycle for LP30+Add, which points to the formation of a more homogeneous CEI layer, as the relatively fast coverage of the active material by a protective layer is key to reduce the electrolyte decomposition at further elevated potentials. The measurements in the P 2p region show a strong increase of the amount of phosphorus surface species during the first charge process for the electrodes tested in LP30+Add, while it stays rather constant for those tested in LP30. This stronger increase in the case of LP30+Add is most probably related to the contribution from TTSPi and its incorporation into the rapidly

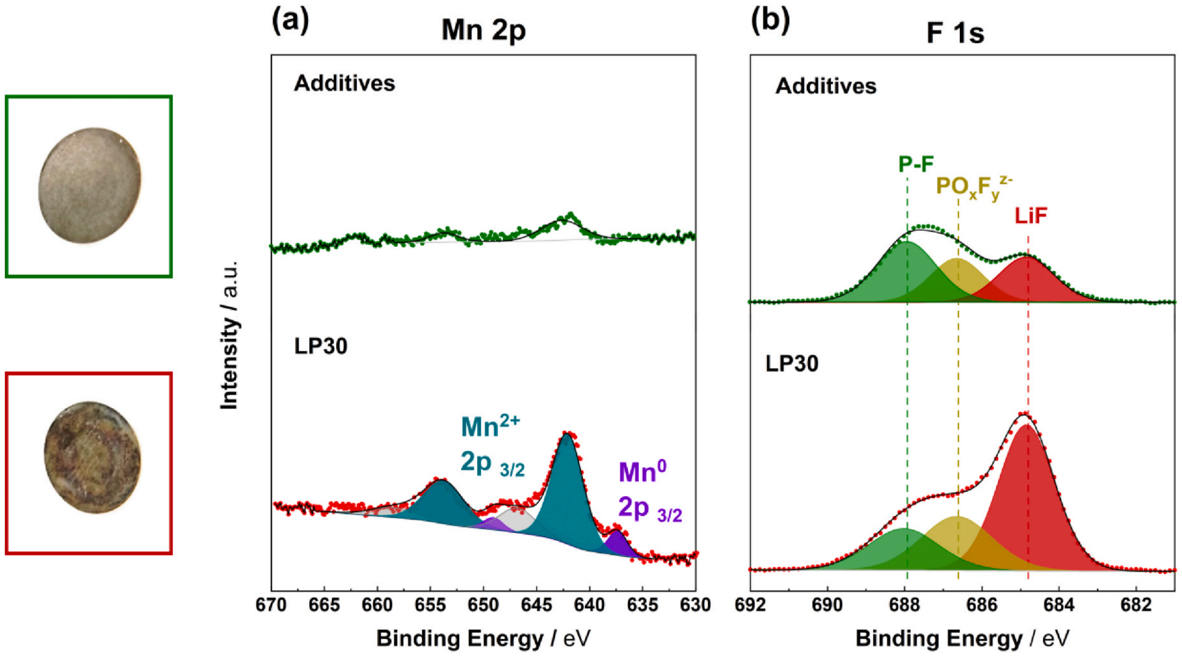

Fig. 3. Left: Photographs of cycled graphite electrodes (with an original diameter of 12 mm) after 300 cycles at C/3 in graphite||LNMO cells with LP30+Add (top, green) and LP30 (bottom, red). (a,b) *Ex situ* XPS analysis of the respective anodes: detail spectra of the (a) Mn 2p and (b) F 1s region after cycling with LP30+Add (top) and LP30 (bottom) as the electrolyte. (For interpretation of the references to color in this figure legend, the reader is referred to the Web version of this article.)

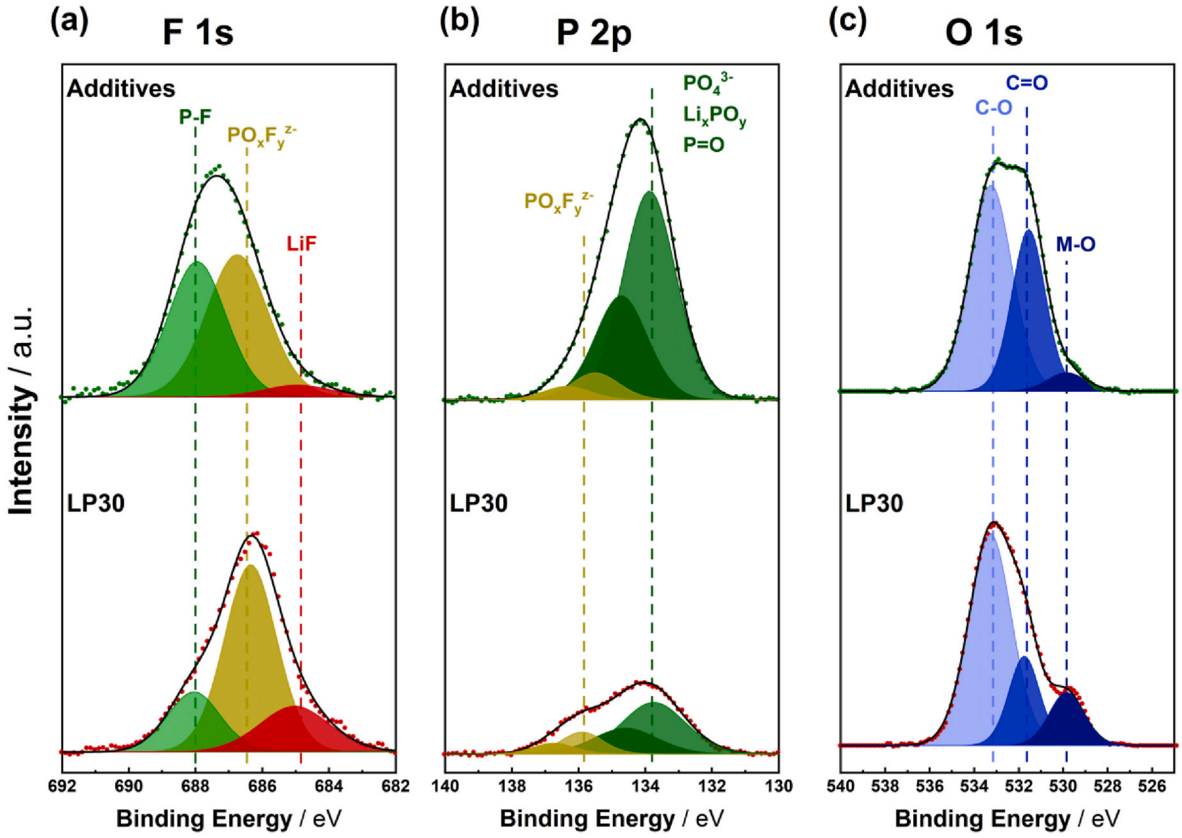

Fig. 4. *Ex situ* XPS analysis of the LNMO electrodes after 300 cycles at C/3 in graphite||LNMO cells. Detail spectra of the (a) F 1s, (b) P 2p, and (c) O 1s regions after cycling with LP30+Add (top) and LP30 (bottom) as the electrolyte.

formed CEI layer. The comparison with electrodes cycled for 300 cycles indicates that the incorporation of TTSPi into the CEI continued upon cycling, as the related signal intensity kept increasing for the LP30+Add electrolyte, while it decreased for LP30, presumably owing to the formation of a rather organic outer CEI in the latter case [67]. The analysis of the B 1s region is complicated by the presence of the P 2s peak(s) in this region, which overlap(s) with the B 1s signals of boron species. Accordingly, features were added into the fit of this region, which represent the P 2s peaks of phosphates (at ~191.6 eV) and $PO_xF_y^{z-}$ (at ~193.5 eV). The intensity of these features is derived from the corresponding P $2p_{3/2}$ peaks by multiplication with the ratio of the relative sensitivity factors of P 2s/P $2p_{3/2}$ (1.1). For the electrodes tested in LP30, this procedure resulted in satisfactory fits; hence, no B 1s signals were detected (as expected). For most of the electrodes tested in LP30+Add, however, an additional peak (at 192 eV) had to be added for a satisfactory fit, reflecting the presence of borate species (cf. Fig. S5). The results show a steadily increasing B concentration on the cathode surface upon cycling (Fig. 5b), indicating an increasing deposition of B-containing species on the LNMO electrodes cycled in LP30+Add. This finding confirms the incorporation of LiBOB fragments into the CEI on LNMO.

Along this line, we would like to note that the voltage profile of the first cycle in LP30+Add containing graphite||LNMO cells (Fig. S6) shows a significant difference in the low potential range: a sloped plateau at about 1.6 V, which appears to be related to the graphite negative electrode. In fact, this additional feature in the voltage profile was also observed in Li||graphite cells (Fig. S7), but vanished from the second cycle on, suggesting that it is related to the initial interphase formation. Since a similar behavior was already reported in the literature as a characteristic feature related to the initial decomposition of LiBOB on graphite electrodes [33,68], further *ex situ* XPS experiments were performed with the recovered graphite electrodes, and the evaluation of the B 1s spectra clearly revealed the presence of (mainly oxidized) boron-containing surface species on the graphite electrode (Fig. S8).

In sum, the *ex situ* XPS analysis revealed that the additives have a significant impact on the interphase formation and composition at both electrodes – the graphite negative electrode and the LNMO positive electrode, thus, suppressing a continuous electrolyte decomposition.

3.3. *Quantification of the gas evolution*

To further investigate the impact of the additives on the initial electrolyte decomposition and, in particular, the formation of gaseous degradation products as an important measure for the potential applicability of this electrolyte composition, we determined the total gas evolving during the initial formation cycles in graphite||LNMO cells. For this purpose, we took advantage of the Archimedes principle, specifically, by correlating the buoyancy of the cell with the voltage profile (from 2.8 to 5.0 V, Fig. 6). As displayed in Fig. 6a, the incorporation of the electrolyte additives results in substantial reduction of the amount of gas formed during the first five (formation) cycles. The gas volume formed in the LP30+Add cell is about 33 % lower at the end of the first dis/-charge cycle and levels off rapidly in the following cycles – in contrast to the continuous gas evolution observed for the LP30 reference cell. The excellent capability of the additive mixture to reduce the electrolyte decomposition, as indicated by the gas evolution, is also depicted by the time-dependent curves in Fig. 6b. While the gas volume is continuously growing in the LP30 cell (red), the volume curve for the LP30+Add cell (green) flattens out very fast. Remarkably, the cell containing the neat LP30 electrolyte shows a continuous gas evolution even when the cycling was stopped, while there is no further gas evolution for LP30+Add. In line with these results, experiments with prolonged cycling show only a very small gas evolution for the LP30+Add cells after the 5th cycle, viz, the gas volume increases by only 0.025 mL

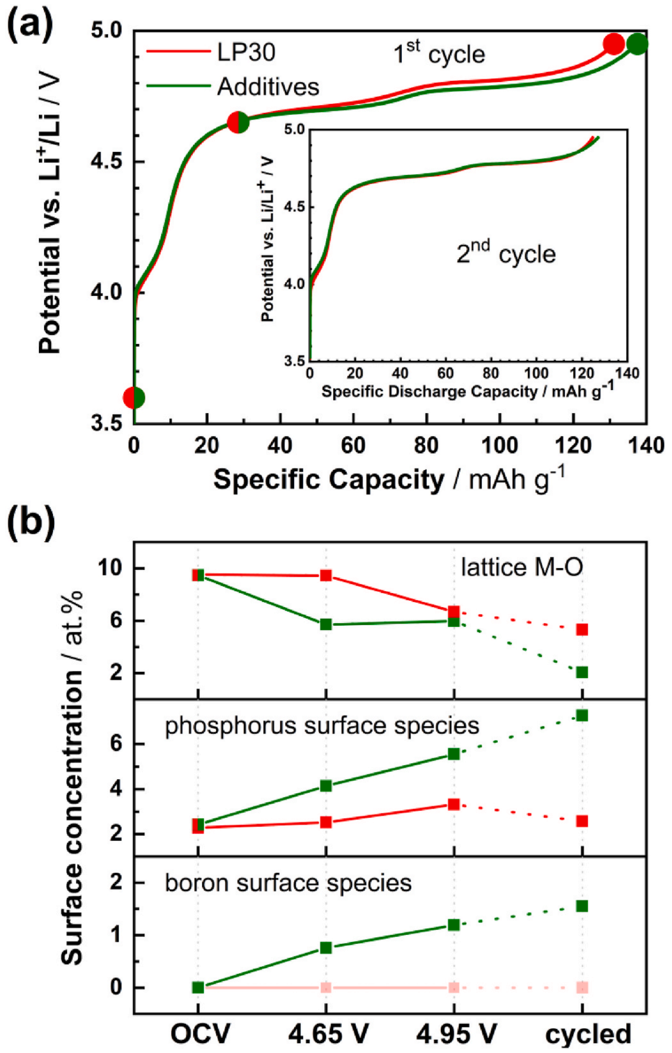

Fig. 5. (a) Comparison of the potential profiles of the first and second (inset) charge half-cycles of Li||LNMO cells with LP30 (red) and LP30+Add (green) as the electrolyte. (b) Evolution of the relative intensity of selected species (see labels) with LP30+Add (green) and LP30 (red) during the first charge cycle from OCV to 4.95 V and after long-term cycling (300 cycles). (For interpretation of the references to color in this figure legend, the reader is referred to the Web version of this article.)

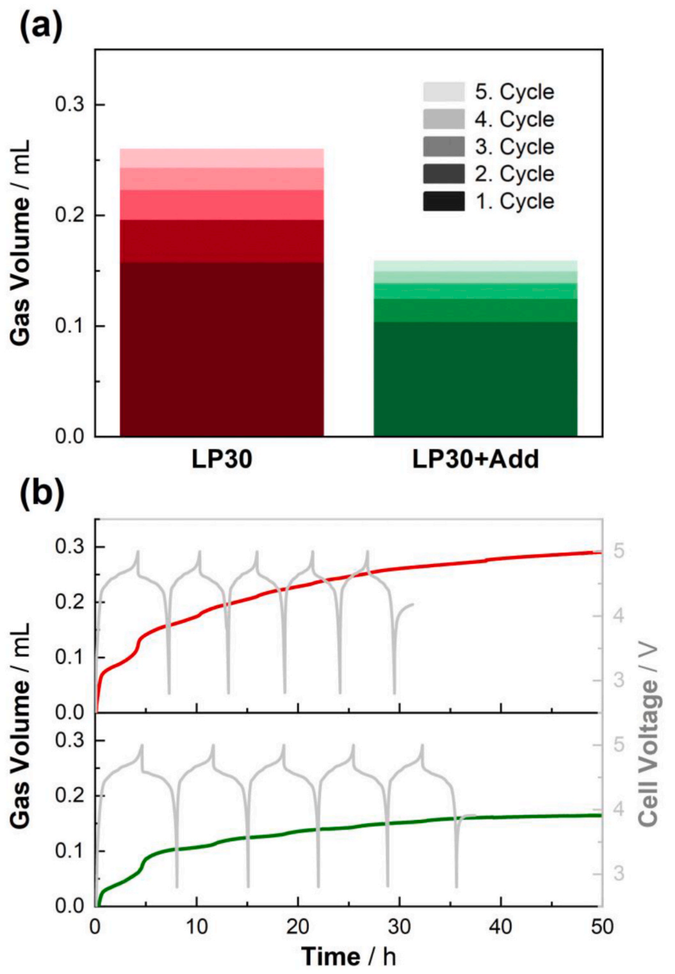

Fig. 6. (a) Cumulative volume of evolved gases during the initial 5 cycles of graphite||LNMO pouch cells using LP30 (red) and P30+Add (green) as the electrolyte. (b) Evolution of the total gas volume and the corresponding cell voltage (grey) versus time. The cells were cycled in the voltage range from 2.8 V to 5.0 V at a dis-/charge rate of C/5. (For interpretation of the references to color in this figure legend, the reader is referred to the Web version of this article.)

between the 5th and 10th cycle (i.e., from 0.15 to 0.175 mL; see. Fig. S9). This substantially faster decrease in gas evolution is highly favorable for the development of optimized formation protocols to enable the commercialization of high-voltage LNMO-based LIBs.

3.4. Differential electrochemical mass spectrometry measurements

A more detailed, qualitative and quantitative analysis of the gas evolution was performed by coupling DEMS and cyclic voltammetry (CV) measurements in a half-cell configuration. In combination with the gas evolution measurements in the previous section, this can also provide information on the chemical nature of the gases formed and the origin of the gas evolution. Using the setup described by Jusys et al. [58], we monitored the evolution of gaseous decomposition products formed at the LNMO electrode during cycling. The resulting CV plots and mass spectrometric traces of the first cycle are presented in Fig S10 and Fig. 7, respectively. The CV plots appear to be rather similar for both electrolytes, both showing the characteristic oxidation and reduction peaks at about 4.8 and 4.3 V, respectively, corresponding to the $Ni^{2+}/Ni^{3+}/Ni^{4+}$ redox reaction, in addition to the redox peaks at about 4.0 V corresponding to the redox activity of manganese [69]. Nevertheless, there are distinct differences. In contrast to the unstructured oxidation peak observed for the LP30 electrolyte in the first cyclic sweep, the typical double peak of the Ni^{2+}/Ni^{4+} redox couple is well resolved in the presence of the additives. Furthermore, the reduction peak appears at a significantly lower potential in LP30 than in the additive containing electrolyte. Even more pronounced are the differences in the subsequent cyclic sweeps. For these, we find a distinct up-shift of the oxidation peak for the LP30 electrolyte, resulting in a broader peak with a maximum at about 5 V. In contrast, for the additive containing electrolyte the oxidation peak maintains its characteristic double peak structure, and also the up-shift is much less pronounced, showing a clear effect of the additives on the CEI stability and ion transport properties.

The mass spectrometric results identified even more significant differences for the gases evolving during the initial CV cycle (Fig. 7). In fact, the background corrected ion current traces obtained for the LP30 electrolyte (Fig. 7, red lines) well resemble previous results [32,58], showing the typical evolution of gaseous H_2, CO, CO_2 and O_2 as represented by the evolution of the $m/z = 2$, 28, 44 and 32 signals, respectively. While the small amount of O_2 is probably extracted from the LNMO lattice, our previous study [58] showed that the presence of Ni^{4+} on the electrode surface can lead to a catalytic dehydrogenation of DMC

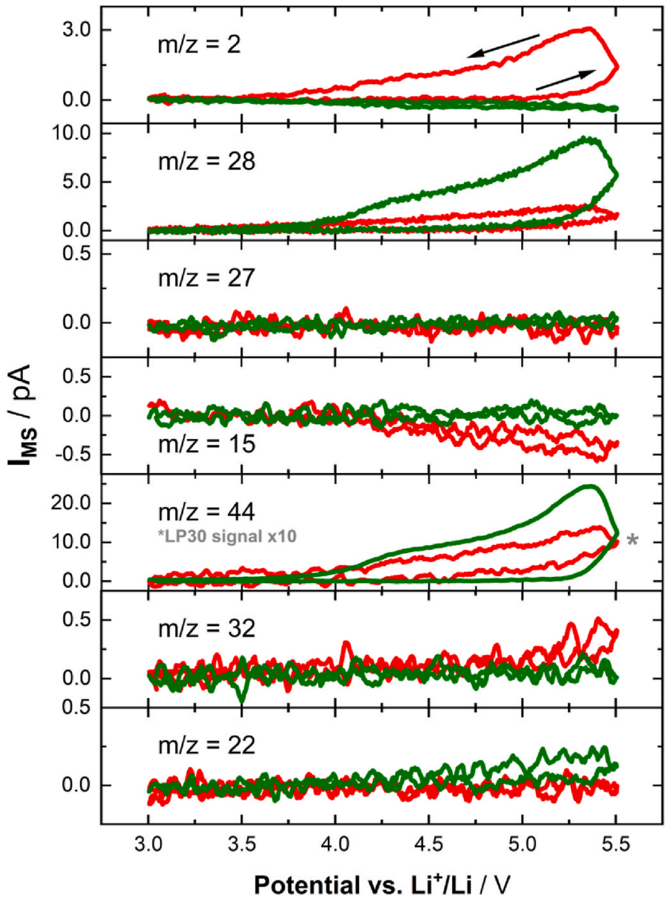

Fig. 7. Selected ion current response (after background subtraction) versus the cell voltage detected via DEMS measurements (v = 2 mV s^{-1}) using Li||LNMO cells with LP30 (red) and LP30+Add (green) as the electrolyte. The $m/z = 44$ signal in LP30 is amplified by a factor of 10, as indicated by the asterisk. (For interpretation of the references to color in this figure legend, the reader is referred to the Web version of this article.)

solvent molecules. Therefore, the carbonates either form oligomers on the electrode surface or decompose to CO and CO_2. The $m/z = 15$ signal (CH_3^+) can be assigned to the major fragment of DMC. Therefore, the decay of the signal may correspond to the consumption of DMC [32,58], though contributions from other organic components cannot be neglected at this mass number, resulting in a complex variation of the background level. The $m/z = 28$ signal may be due to either carbon monoxide (CO) and/or ethylene (C_2H_4). However, as the main fragment of ethylene at $m/z = 27$ [70] remains featureless, the increase of the $m/z = 28$ signal can unambiguously be assigned to CO, though it may partly originate also from CO_2 fragmentation upon electron impact ionization, similar to the double ionized CO_2 at $m/z = 22$ [70].

The gas evolution from the cell employing LP30+Add (Fig. 7, green lines) shows a significantly different behavior. The release of H_2 and the decrease of the DMC background signal ($m/z = 15$) are not observed with this electrolyte, indicating that the additives are able to suppress electrolyte decomposition, which is in very good agreement with the results of our previous study using a binary additive mixture consisting of TTSPi and TFEC [32]. In addition, also the release of O_2 from the lattice is suppressed, underlining the fast formation of a stabilizing electrode|electrolyte interphase thanks to the additives. A clear difference to our previous study on the binary additive mixture [32] is observed for the signals of $m/z = 28$ and 44. In the case of the ternary additive mixture, with LiBOB as third additive, a pronounced evolution of CO and CO_2 gas is observed above 4.0 V which gets even stronger between 5.0 and 5.5 V vs. Li^+/Li. The oxalate based BOB-anion is known to decompose thermally to form gaseous CO and CO_2 [60,71–73]. Consequently, the gas evolution indicates the LiBOB decomposition on LNMO, corroborating the XPS results and, thus, confirming the incorporation of LiBOB derived compounds in the CEI. Nonetheless, the intensity of the CO_2 signal is roughly twice as high as the intensity of the CO signal. Since the relative intensity of the $m/z = 28$ in the fragmentation pattern of CO_2 is only 10 % [70] (compared to $m/z = 44$), most of this signal must originate from actual CO gas formation. This is a major difference to the calculations of Shkrob et al. [73] and the experiments of Xu et al. [60], which suggested a decomposition mechanism exclusively leading to CO_2 gas. However, their proposal of an underlying radical reaction mechanism still represents a plausible explanation, which was also reported in other studies [72,74]. In Fig. 8 (1) we therefore extended the scheme by an additional pathway, taking into account also the CO formation. The resulting boron-containing surface species perfectly match the XPS data, containing not just the detectable boron atoms but also a large number of C=O bonds. In addition to the radical LiBOB decomposition mechanism, it is conceivable that the oxalate moieties (also) decompose via a "Kolbe reaction" [75]. A plausible electrochemical oxidation reaction is depicted in Fig. 8 (2). In fact, such kind of reaction is typically accelerated over metal oxide electrodes [76–78]. This could also explain the steeper increase of the CO_2 signal in the range between 5.0 and 5.5 V ($m/z = 44$ in Fig. 7). Overall, the DEMS data provide unambiguous evidence of CO_2 formation at high potentials in the presence of the three additives, where the oxalate moiety of LiBOB is likely to be oxidized.

4. Conclusion

In this study, we demonstrated the beneficial effect of the ternary additive mixture, consisting of TTSPi, LiBOB and TFEC, on the electrochemical performance of high-voltage LNMO cells in Li-metal and Li-ion configuration and resolved the different mechanisms contributing to it. The improved cycling stability and Coulombic efficiency of the cells is correlated with the incorporation of TTSPi and LiBOB into the CEI and also into the graphite SEI in Li-ion cells. Furthermore, the additives help removing acidic species, e.g., HF, from the electrolyte, thus, drastically reducing transition metal dissolution and manganese migration. Even though the BOB^- decomposition leads to an increased formation of CO_2

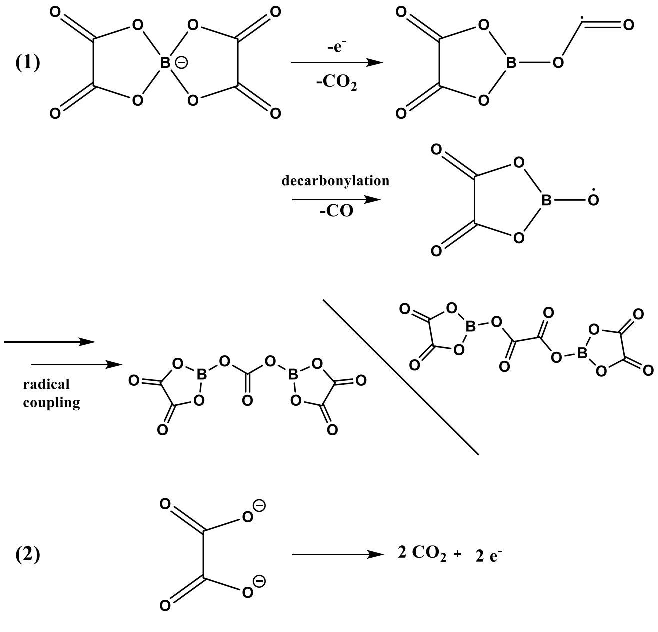

Fig. 8. Schematic depiction of the LiBOB oxidation including the suggested intermediates and main side products. Reaction (1) is a radical oxidation to form surface borates. Reaction (2) is a variant of the Kolbe electrolysis.

and CO gas, the overall gas formation due to electrolyte decomposition decreases substantially for such additive containing electrolyte. In addition, the gas formation decreases rapidly during the initial few cycles and does not continue when the graphite||LNMO cells are at OCV conditions – in stark contrast to the cells containing the additive-free electrolyte. Accordingly, this ternary additive mixture provides a great step forward towards the successful suppression of electrolyte decomposition in such 5 V lithium-ion cells.

CRediT authorship contribution statement

Markus Binder: Writing – original draft, Visualization, Investigation, Formal analysis, Data curation. **Matthias Kuenzel:** Writing – review & editing, Supervision, Methodology, Data curation. **Thomas Diemant:** Writing – review & editing, Investigation, Formal analysis, Data curation. **Zenonas Jusys:** Writing – review & editing, Investigation, Formal analysis, Data curation. **R.Jürgen Behm:** Writing – review & editing, Supervision, Funding acquisition. **Joachim R. Binder:** Writing – review & editing, Resources, Investigation. **Sandro Stock:** Writing – review & editing, Investigation, Data curation. **Felix Diller:** Writing – review & editing, Investigation, Data curation. **Rüdiger Daub:** Writing – review & editing, Supervision, Resources, Funding acquisition. **Stefano Passerini:** Writing – review & editing, Supervision, Methodology, Funding acquisition. **Dominic Bresser:** Writing – review & editing, Writing – original draft, Supervision, Resources, Funding acquisition, Conceptualization.

Declaration of competing interest

The authors declare that they have no known competing financial interests or personal relationships that could have appeared to influence the work reported in this paper.

Acknowledgement

The authors would like to acknowledge financial support from the German Federal Ministry of Education and Research (BMBF) within the ExcellBattUlm (03XP0257D & 03XP0257C) and the ExZellTUM III (03XP0255) project as well as the Helmholtz Association for basic funding. This work contributes to the research performed at CELEST (Center for Electrochemical Energy Storage Ulm-Karlsruhe). The authors would like to thank Daniela Linder for her experimental support during the material synthesis.

Appendix A. Supplementary data

Supplementary data to this article can be found online at https://doi.org/10.1016/j.jpowsour.2024.236073.

Data availability

Data will be made available on request.

References

[1] D. Bradley, Educ. Chem. 47 (2010) 124–125.
[2] X. Zeng, M. Li, D. Abd El-Hady, W. Alshitari, A.S. Al-Bogami, J. Lu, K. Amine, Adv. Energy Mater. 9 (2019) 1–25.
[3] M. Marinaro, D. Bresser, E. Beyer, P. Faguy, K. Hosoi, H. Li, J. Sakovica, K. Amine, M. Wohlfahrt-Mehrens, S. Passerini, J. Power Sources 459 (2020), https://doi.org/10.1016/j.jpowsour.2020.228073.
[4] M. Armand, P. Axmann, D. Bresser, M. Copley, K. Edström, C. Ekberg, D. Guyomard, B. Lestriez, P. Novák, M. Petranikova, W. Porcher, S. Trabesinger, M. Wohlfahrt-Mehrens, H. Zhang, J. Power Sources 479 (2020) 228708.
[5] B.E. Murdock, K.E. Toghill, N. Tapia-Ruiz, Adv. Energy Mater. 11 (2021) 2102028.
[6] M. Greenwood, M. Wentker, J. Leker, J. Power Sources Adv 9 (2021) 100055.
[7] D. Bresser, D. Buchholz, A. Moretti, A. Varzi, S. Passerini, Energy Environ. Sci. 11 (2018) 3096–3127.
[8] X. Yu, W.A. Yu, A. Manthiram, Small Methods 5 (2021) 1–30.
[9] J.H. Kim, N.P.W. Pieczonka, L. Yang, ChemPhysChem 15 (2014) 1940–1954.
[10] G. Liang, V.K. Peterson, K.W. See, Z. Guo, W.K. Pang, J. Mater. Chem. A 8 (2020) 15373–15398.
[11] J. Asenbauer, T. Eisenmann, M. Kuenzel, A. Kazzazi, Z. Chen, D. Bresser, Sustain. Energy Fuels 4 (2020) 5387–5416.
[12] X.Y. Fan, M. Liu, T.L. Chen, W. Hao, Z. Cao, N. Jiang, Q. Liu, Y.H. Feng, H. Qin, S. F. Chen, S. Liu, X. Ji, Y. Xiao, S. Chou, P.F. Wang, Adv. Funct. Mater. 2400996 (2024) 1–12.
[13] J.C. Hestenes, J.T. Sadowski, R. May, L.E. Marbella, ACS Mater. Au 3 (2023) 88–101.
[14] X. Fan, C. Wang, Chem. Soc. Rev. 50 (2021) 10486–10566.
[15] T. Yoon, J. Soon, T.J. Lee, J.H. Ryu, S.M. Oh, J. Power Sources 503 (2021) 230051.
[16] Y.M. Song, J.G. Han, S. Park, K.T. Lee, N.S. Choi, J. Mater. Chem. A 2 (2014) 9506–9513.
[17] Y.M. Song, C.K. Kim, K.E. Kim, S.Y. Hong, N.S. Choi, J. Power Sources 302 (2016) 22–30.
[18] N.P.W.W. Pieczonka, Z. Liu, P. Lu, K.L. Olson, J. Moote, B.R. Powell, J.-H.H. Kim, J. Phys. Chem. C 117 (2013) 15947–15957.
[19] M.S. Milien, H. Beyer, W. Beichel, P. Klose, H.A. Gasteiger, B.L. Lucht, I. Krossing, J. Electrochem. Soc. 165 (2018) A2569–A2576.
[20] J.H. Kim, N.P.W. Pieczonka, Z. Li, Y. Wu, S. Harris, B.R. Powell, Electrochim. Acta 90 (2013) 556–562.
[21] B. Michalak, B.B. Berkes, H. Sommer, T. Brezesinski, J. Janek, J. Phys. Chem. C 121 (2017) 211–216.
[22] M.D. Bhatt, C. O`Dwyer, Chem. Phys. Lett. 618 (2015) 208–213.
[23] S. Tan, Y.J. Ji, Z.R. Zhang, Y. Yang, ChemPhysChem 15 (2014) 1956–1969.
[24] S. Chen, K. Wen, J. Fan, Y. Bando, D. Golberg, J. Mater. Chem. A 6 (2018) 11631–11663.
[25] X. Zheng, Y. Liao, Z. Zhang, J. Zhu, F. Ren, H. He, J. Energy Chem. 42 (2020) 62–70.
[26] J. Kalhoff, G.G. Eshetu, D. Bresser, S. Passerini, ChemSusChem 8 (2015) 2154–2175.
[27] N. Xu, J. Shi, G. Liu, X. Yang, J. Zheng, Z. Zhang, Y. Yang, J. Power Sources Adv 7 (2021) 100043.
[28] Y.K. Han, J. Yoo, T. Yim, J. Mater. Chem. A 3 (2015) 10900–10909.
[29] N.N. Sinha, J.C. Burns, J.R. Dahn, J. Electrochem. Soc. 161 (2014) A1084–A1089.
[30] S. Mai, M. Xu, X. Liao, J. Hu, H. Lin, L. Xing, Y. Liao, X. Li, W. Li, Electrochim. Acta 147 (2014) 565–571.
[31] L. Ma, J. Xia, J.R. Dahn, J. Electrochem. Soc. 162 (2015) A1170–A1174.
[32] A. Kazzazi, D. Bresser, M. Kuenzel, M. Hekmatfar, J. Schnaidt, Z. Jusys, T. Diemant, R.J. Behm, M. Copley, K. Maranski, J. Cookson, I. de Meatza, P. Axmann, M. Wohlfahrt-Mehrens, S. Passerini, J. Power Sources 482 (2021) 228975.
[33] C. Täubert, M. Fleischhammer, M. Wohlfahrt-Mehrens, U. Wietelmann, T. Buhrmester, J. Electrochem. Soc. 157 (2010) A721.
[34] N.P.W. Pieczonka, L. Yang, M.P. Balogh, B.R. Powell, K. Chemelewski, A. Manthiram, S.A. Krachkovskiy, G.R. Goward, M. Liu, J.H. Kim, J. Phys. Chem. C 117 (2013) 22603–22612.
[35] M.Y. Abeywardana, N. Laszczynski, M. Kuenzel, D. Bresser, S. Passerini, B. Lucht, Int. J. Electrochem. 2019 (2019) 1–7.
[36] S. Dalavi, M. Xu, B. Knight, B.L. Lucht, Electrochem. Solid State Lett. 15 (2012) 28–31.
[37] Y. Dong, B.T. Young, Y. Zhang, T. Yoon, D.R. Heskett, Y. Hu, B.L. Lucht, ACS Appl. Mater. Interfaces 9 (2017) 20467–20475.
[38] S.Y. Ha, J.G. Han, Y.M. Song, M.J. Chun, S. Il Han, W.C. Shin, N.S. Choi, Electrochim. Acta 104 (2013) 170–177.
[39] Y. Sasaki, Fluorinated Mater. Energy Convers. (2005) 285–304.
[40] M. Bolloli, F. Alloin, J. Kalhoff, D. Bresser, S. Passerini, P. Judeinstein, J. C. Leprêtre, J.Y. Sanchez, Electrochim. Acta 161 (2015) 159–170.
[41] K.C. Möller, T. Hodal, W.K. Appel, M. Winter, J.O. Besenhard, J. Power Sources 97–98 (2001) 595–597.
[42] J. Xia, R. Petibon, A. Xiao, W.M. Lamanna, J.R. Dahn, J. Electrochem. Soc. 163 (2016) A1637–A1645.
[43] J. Kalhoff, D. Bresser, M. Bolloli, F. Alloin, J.Y. Sanchez, S. Passerini, ChemSusChem 7 (2014) 2939–2946.
[44] J. Im, J. Lee, M.-H. Ryou, Y.M. Lee, K.Y. Cho, J. Electrochem. Soc. 164 (2017) A6381–A6385.
[45] B. Wu, Y. Ren, D. Mu, X. Liu, J. Zhao, F. Wu, J. Solid State Electrochem. 17 (2013) 811–816.
[46] C. Xu, F. Lindgren, B. Philippe, M. Gorgoi, F. Björefors, K. Edström, T. Gustafsson, Chem. Mater. 27 (2015) 2591–2599.
[47] Z. Fang, Z. Zheng, W. Cheng, X. Zhang, K. Zhong, L. Li, Front. Chem. 8 (2020) 1–10.
[48] W. Song, R. Gauthier, T. Taskovic, D. Ouyang, H.A. Ingham, A. Eldesoky, S. M. Azam, E.S. Zsoldos, Z. Deng, D.H. Heino, C. Geng, R. Sidebottom, J.R. Dahn, J. Electrochem. Soc. 169 (2022) 110513.
[49] A. Höweling, D. Stenzel, H. Gesswein, M. Kaus, S. Indris, T. Bergfeldt, J.R. Binder, J. Power Sources 315 (2016) 269–276.
[50] A. Höweling, A. Stoll, D.O. Schmidt, H. Geßwein, U. Simon, J.R. Binder, J. Electrochem. Soc. 164 (2017) A6349–A6358.
[51] M. Kuenzel, H. Choi, F. Wu, A. Kazzazi, P. Axmann, M. Wohlfahrt-Mehrens, D. Bresser, S. Passerini, ChemSusChem 13 (2020) 2650–2660.
[52] M. Kuenzel, D. Bresser, T. Diemant, D.V. Carvalho, G.T. Kim, R.J. Behm, S. Passerini, ChemSusChem 11 (2018) 562–573.
[53] N. Loeffler, G.T. Kim, F. Mueller, T. Diemant, J.K. Kim, R.J. Behm, S. Passerini, ChemSusChem 9 (2016) 1112–1117.

[54] C.P. Aiken, J. Xia, D.Y. Wang, D.A. Stevens, S. Trussler, J.R. Dahn, J. Electrochem. Soc. 161 (2014) A1548–A1554.

[55] C.P. Aiken, J. Self, R. Petibon, X. Xia, J.M. Paulsen, J.R. Dahn, J. Electrochem. Soc. 162 (2015) A760–A767.

[56] S. Stock, F. Diller, J. Böhm, L. Hille, J. Hagemeister, A. Sommer, R. Daub, J. Electrochem. Soc. 170 (2023) 060539.

[57] S. Stock, J. Böhm, M. Ank, P. Rath, M. Lienkamp, R. Daub, J. Power Sources 613 (2024) 234858.

[58] Z. Jusys, M. Binder, J. Schnaidt, R.J. Behm, Electrochim. Acta 314 (2019) 188–201.

[59] E. Wood, M. Alexander, T.H. Bradley, J. Power Sources 196 (2011) 5147–5154.

[60] M. Xu, N. Tsiouvaras, A. Garsuch, H.A. Gasteiger, B.L. Lucht, J. Phys. Chem. C 118 (2014) 7363–7368.

[61] M. Xu, L. Zhou, Y. Dong, Y. Chen, A. Garsuch, B.L. Lucht, J. Electrochem. Soc. 160 (2013) A2005–A2013.

[62] M. Lin, L. Ben, Y. Sun, H. Wang, Z. Yang, L. Gu, X. Yu, X. Yang, H. Zhao, R. Yu, M. Armand, X. Huang, Chem. Mater. 27 (2015) 292–303.

[63] D. Wang, C. Gao, X. Zhou, S. Peng, M. Tang, Y. Wang, L. Huang, W. Yang, X. Gao, Carbon Energy 1–9 (2023).

[64] M. Genovese, A.J. Louli, R. Weber, S. Hames, J.R. Dahn, J. Electrochem. Soc. 165 (2018) A3321–A3325.

[65] X.Q. Zhang, X.B. Cheng, X. Chen, C. Yan, Q. Zhang, Adv. Funct. Mater. 27 (2017) 1–8.

[66] Q. Li, Y. Wang, X. Wang, X. Sun, J.N. Zhang, X. Yu, H. Li, ACS Appl. Mater. Interfaces 12 (2020) 2319–2326.

[67] J. C. Hestenes, L. E. Marbella, 2023, c, DOI 10.1021/acsenergylett.3c01529..

[68] X. Cui, H. Zhang, S. Li, X. Li, H. Feng, Ionics 20 (2014) 789–794.

[69] M.T. Nguyen, H.Q. Pham, J.A. Berrocal, I. Gunkel, U. Steiner, J. Mater. Chem. A 11 (2023) 7670–7678.

[70] P.J. Linstrom, W.G. Mallard, Mass Spectra' in NIST Chemistry WebBook, National Institute Of Standards And Technology, Gaithersburg, 2010.

[71] E. Zinigrad, L. Larush-Asraf, G. Salitra, M. Sprecher, D. Aurbach, Thermochim. Acta 457 (2007) 64–69.

[72] Y. Wang, L. Xing, X. Tang, X. Li, W. Li, B. Li, W. Huang, H. Zhou, X. Li, RSC Adv. 4 (2014) 33301–33306.

[73] I.A. Shkrob, Y. Zhu, T.W. Marin, D.P. Abraham, J. Phys. Chem. C 117 (2013) 23750–23756.

[74] Z. Xiao, J. Liu, G. Fan, M. Yu, J. Liu, X. Gou, M. Yuan, F. Cheng, Mater. Chem. Front. 4 (2020) 1689–1696.

[75] A.K. Vijh, B.E. Conway, Chem. Rev. 67 (1967) 611–622.

[76] S. Ferro, C.A. Martínez-Huitle, A. De Battisti, J. Appl. Electrochem. 40 (2010) 1779–1787.

[77] O. Kosohin, V. Mazanka, J. Chem. Technol. Metall. 57 (2022) 137–140.

[78] S. Solchenbach, M. Wetjen, D. Pritzl, K.U. Schwenke, H.A. Gasteiger, J. Electrochem. Soc. 165 (2018) A512–A524.